Article

Not peer-reviewed version

$[Fe^{III}Cl(TMPPH_2)][Fe^{III}Cl_4]_2$: A Stand-Alone Molecular Nanomedicine that Induces High Cytotoxicity by Ferroptosis

Xiao Wang *, Jia-Hao Feng, Chun-Mei Zeng, Ze-Sheng Zhang, Feng-Lin Cao, Wen-Hua Zhang *, Jin-Xiang Chen, Yiming Mao, David James Young

Posted Date: 29 April 2024

doi: 10.20944/preprints202404.1891.v1

Keywords: single-molecular nanomedicine; porphyrin ligand; chemodynamic therapy; ferroptosis; breast cancer therapy

 doi:10.20944/preprints202404.1891.v1

Article

$[Fe^{III}Cl(TMPPH_2)][Fe^{III}Cl_4]_2$: A Stand-Alone Molecular Nanomedicine that Induces High Cytotoxicity by Ferroptosis

Xiao Wang [1,#], Jia-Hao Feng [2,#], Chun-Mei Zeng [1], Ze-Sheng Zhang [1], Feng-Lin Cao [1], Wen-Hua Zhang [1,*], Jin-Xiang Chen [2,*], Yiming Mao [3,*] and David J. Young [4]

[1] College of Chemistry, Chemical Engineering, and Materials Science, Soochow University, Suzhou 215123, China
[2] NMPA Key Laboratory for Research and Evaluation of Drug Metabolism, Guangdong Provincial Key Laboratory of New Drug Screening, School of Pharmaceutical Sciences, Southern Medical University, Guangzhou 510515, China
[3] Department of Thoracic Surgery, Suzhou Kowloon Hospital, Shanghai Jiaotong University School of Medicine, Suzhou 215021, China.
[4] Glasgow College UESTC, University of Electronic Science and Technology of China, Chengdu 611731, China
* Correspondence: whzhang@suda.edu.cn (W.-H.Z.); jxchen@smu.edu.cn (J.-X.C.); mym19850126@163.com (Y.M.)
[#] These authors contributed equally to this work

Abstract: Developing clinically meaningful nanomedicines for cancer therapy requires the drugs to be effective, safe, simple, cheap, and easy to store. In the present work, we report that a simple cationic Fe(III)-rich salt of $[Fe^{III}Cl(TMPPH_2)][Fe^{III}Cl_4]_2$ (**Fe-TMPP**) exhibits a superior anticancer performance toward a broad spectrum of cancer cell lines, including breast, colorectal cancer, liver, pancreatic, prostate, and gastric cancers, with half maximal inhibitory concentration (IC_{50}) values in the range of 0.098–3.97 μM (0.066–2.68 μg mL^{-1}), and comparable to the best-reported medicines. **Fe-TMPP** can forms stand-alone nanoparticles in water without the need for extra surface modification or organic-solvent-assisted antisolvent precipitation. Critically, **Fe-TMPP** is TME-responsive (TME = tumor microenvironment), and can only elicit its function in the TME with overexpressed H_2O_2, converting H_2O_2 to the cytotoxic •OH to oxidize the phospholipid of the cancer cell membrane, causing ferroptosis, a programmed cell death process of cancer cells.

Keywords: single-molecular nanomedicine; porphyrin ligand; chemodynamic therapy; ferroptosis; breast cancer therapy

1. Introduction

Materials designed to target the unique features of the tumor microenvironment (TME), such as the over-expression of H_2O_2 and glutathione (GSH), weak acidity, hypoxia, and immunosuppression, are attracting intensive interest in the field of nanomedicine.[1–6] On the one hand, materials that are responsive exclusively to the TME imply low systemic toxicity and thus fewer side effects. On the other hand, disturbing the complex homeostasis of the TME may result in effective cancer therapy by novel cell death modalities (e.g., ferroptosis, pyroptosis, and immunogenic cell death),[7–9] and the resensitization of cells to conventional therapies.[2,9,10] Nevertheless, most of the current formulations are far from satisfactory for practical use due to their formidable structural complexity, high cost, and low cellular uptake that subsequently leads to low anticancer efficacy.

Some useful strategies have been proposed to promote cellular uptake and accumulation of the drugs in organelles (particularly mitochondria),[11,12] and the synergistic operation between different therapeutic modalities, such as chemotherapy, chemodynamic therapy (CDT), and photodynamic therapy (PDT), by taking advantage of the chemical properties of individual building

 doi:10.20944/preprints202404.1891.v1

blocks of the nanomedicine. For example, Ke et al. have designed a cyclometallated Ir(III) complex featuring a −SH terminal as the cationic and photoactive building block.[13] Upon polymerization by disulfide bond formation, followed by DSPE-PEG-Biotin coating to endow aqueous solubility and cell specificity, the particle (denoted as IrS NPs) could be used for TME-responsive cancer therapy by harnessing both apoptosis and ferroptosis pathways. When IrS NPs were taken up by the cells, the disulfide bond was cleavaged by cross-coupling with the intracellular GSH to release the cationic subcomponent, which in turn, selectively accumulated in mitochondria. Notably, the use of Ir(III)-based photosensitizers elicited type I PDT which circumvented the need for molecular oxygen. The oxidative stress imposed by the generated reactive oxygen species (ROS) from PDT resulted in apoptosis of the lung cancer A549 cell line, while the depletion of GSH by IrS NPs weakened the reductive defense of the cells, leading to the effective peroxidation of the phospholipid, causing ferroptosis. In a similar effort, Yuan et al. designed a small molecular drug MitoIrL2 featuring a cyclometallated Ir(III) skeleton for the hybrid treatment of breast and pancreatic cancer via a shared mechanism (apoptosis from type I PDT and ferroptosis).[14] In MitoIrL2, the presence of an additional cationic phosphonium center resulted in more efficient mitochondrial accumulation and therefore better treatment outcomes relative to its phosphonium-free counterpart.

In the present work, we report that a simple salt of $[Fe^{III}Cl(TMPPH_2)][Fe^{III}Cl_4]_2$ (denoted as **Fe-TMPP**; $TMPPH_2$ is used to differentiate the ligand from the free-base porphyrin precursor of *meso*-tetrakis (6-methylpyridin-3-yl) porphyrin, H_2TMPP) exhibits superior cytotoxicity towards a broad spectrum of cancer cell lines, including 4T1 (breast cancer), HCT-116 (colorectal cancer), DLD-1 (colorectal cancer), HuH-7 (liver cancer), BXPC3 (pancreatic cancer), PC3 (prostate cancer), and AGS (gastric cancer), with half maximal inhibitory concentration (IC_{50}) values in the range 0.098−3.97 μM (0.066−2.68 μg mL^{-1}), comparable to the best-reported medicines including cisplatin and those exhibiting multiple treatment modalities.

2. Results and Discussion

2.1. Material Synthesis and Structure Descriptions

The assembly of $FeCl_3·6H_2O$ and H_2TMPP under solvothermal conditions in $CHCl_3$/EtOH using HAc as the modulating reagent resulted in the formation of **Fe-TMPP**. The successful synthesis was authenticated by single-crystal X-ray crystallographic analysis. **Fe-TMPP** crystallizes in the triclinic space group *P*−1 (Table 1), featuring a cation of $[Fe^{III}Cl(TMPPH_2)]^{2+}$ and a pair of $[FeCl_4]^-$ counterions (Figure 1a). The $[Fe^{III}Cl(TMPPH_2)]^{2+}$ cation features a 'sit-atop' Fe^{3+} which is chelated by four of the N atoms from the H_2TMPP ligand and one Cl^- to give a five-coordinate square pyramidal configuration. Notably, of the four methylpyridyl peripheries of the H_2TMPP ligand, the two N at the para-positions are protonated, as suggested by the presence of two $[FeCl_4]^-$ ions for each $[Fe^{III}Cl(TMPPH_2)]^{2+}$ cation in addition to the relative dispositions of these methylpyridyl moieties in the molecular packing diagram (Figure S1). Structure refined with full protonation of the methylpyridyl N sites or misplaced protons inevitably led to short H···H contacts.

 doi:10.20944/preprints202404.1891.v1

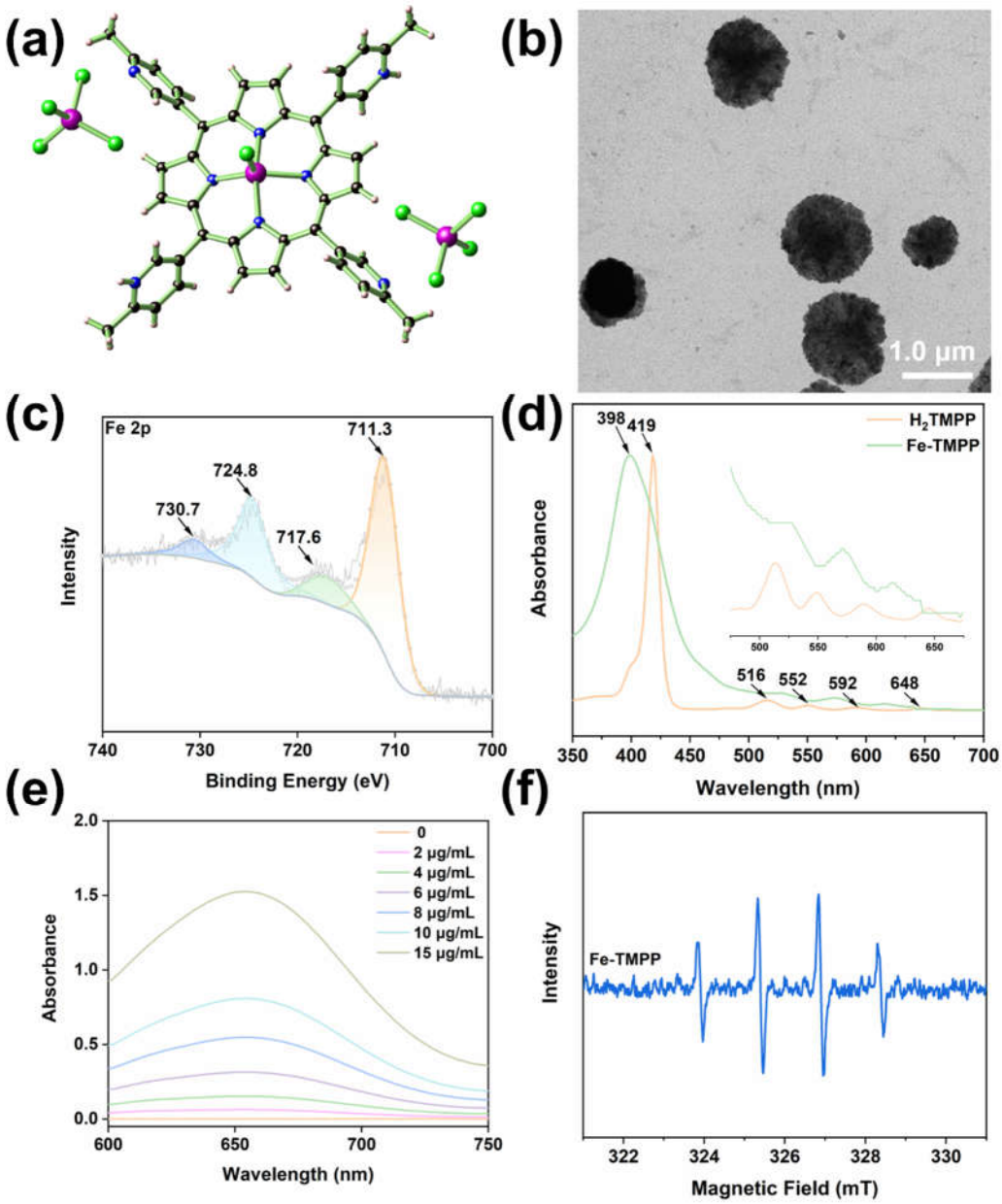

Figure 1. The crystal structure of **Fe-TMPP** with the disordered domain omitted for clarity (a; Fe dark magenta, Cl green, N blue, C black, H light pink). TEM image (b) and the Fe 2p XPS spectra (c) of **Fe-TMPP**. A comparison of the UV-Vis spectra of H_2TMPP (in DMF) and **Fe-TMPP** (in water) (d; inset: the absorption in the range of 475−675 nm as amplified 10 times). Change of UV-Vis absorption intensity at 652 nm (oxTMB) upon treatment with different concentrations of **Fe-TMPP** in the presence of 100 μM H_2O_2 (e). EPR spectrum showing •OH production from H_2O_2 as induced by **Fe-TMPP** with DMPO as the spin trap (f).

 doi:10.20944/preprints202404.1891.v1

Table 1. Crystal data and structure refinement parameters for **Fe-TMPP**.

	Fe-TMPP
CCDC number	2330690
Formula	$C_{44}H_{34}Cl_9Fe_3N_8$
Formula weight	1161.39
Crystal system	Triclinic
Space group	*P*-1
a/Å	9.5980(6)
b/Å	11.0408(7)
c/Å	14.4682(10)
α/°	70.702(3)
β/°	86.792(3)
γ/°	75.171(2)
V/Å^3	1398.16(16)
Z	1
D_c/(g cm^{-3})	1.379
F(000)	585
μ (Mo–Kα)/mm^{-1}	1.234
Total reflections	29635
Unique reflections	4006
Observed reflections	2844
No parameters	339
R_{int}	0.0778
R^a	0.1007
wR^b	0.2811
GOF^c	1.055

$^aR = \Sigma||F_o|-|F_c||/\Sigma|F_o|$. $^bwR = \{\Sigma w(F_o^2-F_c^2)^2/\Sigma w(F_o^2)^2\}^{1/2}$. ^{c}GOF = $\{\Sigma w((F_o^2-F_c^2)^2)]/(n-p)\}^{1/2}$, where n = number of reflections, p = total number of parameters refined.

2.2. Spectroscopic Characterizations of Fe-TMPP

Fe-TMPP was spectroscopically characterized and compared with its H_2TMPP precursor. The in-plane N-H vibration at 964 cm^{-1} in the Fourier-transform infrared (FT-IR) spectrum of the ligand disappeared (Figure S2), and a new peak at 997 cm^{-1} appeared in **Fe-TMPP**, indicating metallation of the porphyrin center. Fe 2p X-ray photoelectron spectroscopy (XPS) of **Fe-TMPP** revealed two peaks at binding energies of 711.3 eV and 724.8 eV which are assignable by the spin-orbit splitting of the Fe $2p_{3/2}$ and Fe $2p_{1/2}$ of Fe^{3+} (Figure 1c), while a pair of satellite peaks at around 717.6 eV and 730.7 eV were also present, presumably due to the photoreduction of Fe^{3+} during the measurement.[15,16]

In the ultraviolet-visible (UV-Vis) spectra (Figure 1d), the Soret band of the free H_2TMPP at 419 nm underwent a significant blueshift to 398 nm upon chelation of Fe^{3+}. In addition, the Q bands coalesced into two, due to the change of symmetry from D_{2h} of H_2TMPP to C_{4v} of Fe-TMPP.[17,18] Notably, an additional absorption band at around 650 nm also appeared, presumably due to the charge transfer between Fe^{3+} and the ligand.[19] Notably, the UV-Vis spectrum of **Fe-TMPP** exhibited an undulating baseline, indicating lighting scattering by nanoparticle formation in an aqueous solution.[20] The formation of a stand-alone nanoparticle of **Fe-TMPP** could be directly observed by the Tyndall effect (Figure S3). Energy dispersive X-ray spectroscopy (EDS) showed an Fe: Cl : N atomic ratio of 1.0 : 2.6 : 3.0 in **Fe-TMPP** (Figure S4a), which is close to the value of 1.0 : 3.0 : 2.7 found in the single crystal data.

 doi:10.20944/preprints202404.1891.v1

2.3. Characterizations of Fe-TMPP Nanoparticles

The direct nanoparticle formation of **Fe-TMPP** in water was observed in the transmission electron microscopic (TEM) images and also by dynamic light scattering (DLS) analysis. TEM showed that **Fe-TMPP** formed particles of variable sizes (Figure 1b). DLS gave different results from batch to batch but all contained considerable numbers of particles with sizes less than 100 nm (Figure S5). We argue that the accuracy of the TEM results may be compromised as the particles of **Fe-TMPP** without any surface modification may undergo an Ostwald ripening process upon solvent evaporation during sample preparation.[21] The zeta potential of **Fe-TMPP** was 23.4 mV (Figure S6), which is ideal for ensuring good circulation stability with favorable adhesion to cell membranes for enhanced intracellular uptake.[22]

Nanoparticles can be assembled and stored in an aqueous solution for short periods, or lyophilized for longer-term preservation. However, lyophilized particles can change their morphology, aggregate, or slowly degrade.[23,24] Antisolvent precipitation is an often-used alternative to prepare nanoparticles of organic drugs. A risk with this approach, however, is encapsulation of toxic organic solvents, and sometimes the need for a supercritical antisolvent (e.g., CO_2).[25,26] The simple chemical formulation and good water-dispersing ability of **Fe-TMPP** is thus an advantage for storage and facile particle preparation.

Fresh samples of **Fe-TMPP** in aqueous solutions maintained their color and homogeneity under ambient conditions for three days (Figure S7), as also evidenced by their UV-Vis spectra (Figure S8). In addition, **Fe-TMPP** was stable in PBS (0.1x) for 0, 12, and 24 hours, as indicated by only insignificant changes in particle size (Figure S9) and zeta potential (Figure S10). To further confirm the stability of **Fe-TMPP** in water, we sonicated the aqueous suspensions of **Fe-TMPP** and then lyophilized. The powder X-ray diffraction (PXRD) analysis revealed that the diffraction patterns of the water-treated samples resembled that of the as-synthesized crystalline samples (Figure S11). Moreover, the EDS spectra of the lyophilized sample of **Fe-TMPP** showed an Fe: Cl : N atomic ratio of 1.0 : 2.4 : 3.2 (Figure S4b), which was close to that of the as-synthesized crystalline sample (1.0 : 2.6 : 3.0), indicating that there was no obvious compositional change upon suspending **Fe-TMPP** in water. We postulate that the four methyl groups at the ortho position of the pyridyl N sites significantly boost the hydrophobicity of the molecule to facilitate the aggregation of the polar **Fe-TMPP** featuring multiple hydrophilic moieties (i.e., $[FeCl_4]^-$, protonated pyridyl ligands, the Fe-Cl, and free pyridyl N site) and thereby protecting the salt from hydrolyzation.

2.4. Detection Fe-TMPP-Induced Generation of ROS in Solution

High valent transition metal ions Fe^{3+} and Cu^{2+} exhibit peroxidase-like activity to generate reactive •OH by utilizing the overexpressed H_2O_2 in the TME, thereby eliciting nonspecific damage inside cancer cells.[6–8,17] The TME also reduces Fe^{3+} and Cu^{2+} to Fe^{2+} and Cu^{+} by reaction with the overexpressed GSH to initiate Fenton and Fenton-like reactions, which also generate •OH from H_2O_2. The peroxidase-like activity of the Fe^{3+}-rich **Fe-TMPP** was therefore assayed using 3,3′,5,5′-tetramethylbenzidine (TMB).[27] Different concentrations of **Fe-TMPP** were added to TMB solutions containing 100 μM H_2O_2, the approximate concentration in tumors, and five times higher than in normal cells.[1,2] It can be seen from Figure 1e that **Fe-TMPP** produced considerable •OH in a concentration-dependent manner upon incubating with H_2O_2 over 3 hours. The generation of •OH was confirmed by electron paramagnetic resonance (EPR) spectroscopy using DMPO as the spin trap. As shown in Figure 1f, the EPR spectrum of **Fe-TMPP** gave rise to a strong four-line signal with a 1:2:2:1 peak-to-peak intensity pattern, characteristic of the generation of •OH from H_2O_2.[4,5]

Fe-TMPP is supported by a porphyrin-based ligand, which is often used for type II PDT of cancer.[3,7,28] We employed diphenylisobenzofuran (DPBF) as a probe to compare the singlet oxygen ($^1O_2$) generating capacity with that of **TMPP-F127** (H_2TMPP encapsured by Pluronic F-127, Figure S12),[29] using blank DPBF as a control.[30,31] DPBF was added to aqueous solutions of **TMPP-F127** and **Fe-TMPP**, followed by laser irradiation (650 nm, 25 mW cm^{-2}). As shown in Figure S13, at equivalent H_2TMPP concentrations, neither species could generate sufficient $^1O_2$ to degrade DPBF under laser irradiation. The $^1O_2$ generated by **Fe-TMPP** was negligible, which might be due to

 doi:10.20944/preprints202404.1891.v1

the presence of redox-active Fe^{3+} that can quench the excited state of the molecule by electron transfer.[32,33]

2.5. In Vitro ROS Detection and Cytotoxicity Assay

Given the efficient •OH production in water induced by **Fe-TMPP**, we next investigated in vitro ROS generation by **Fe-TMPP** in the representative 4T1 cell line using 2′,7′-dichlorodihydrofluorescein diacetate (DCFH-DA) as a fluorescence probe.[4] As shown in Figure 2a and Figure S14, green fluorescence was detected in the cells treated with **Fe-TMPP**, which indicated the production of ROS in the cells from the peroxidase-like activity of Fe^{3+}. By comparison, **TMPP-F127** produced little ROS, which may be due to the aggregation of the H_2TMPP ligand within the hydrophobic core of the **TMPP-F127** micelles.

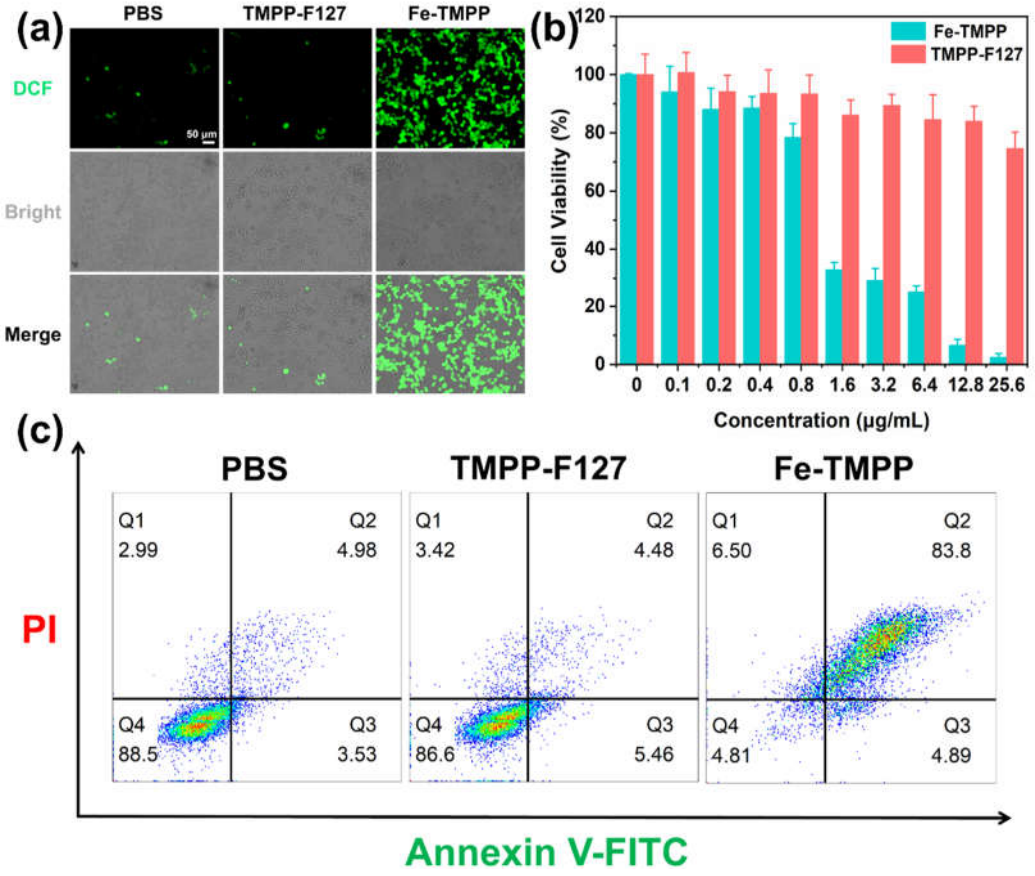

Figure 2. The generation of intracellular ROS by **TMPP-F127**, **Fe-TMPP**, and PBS control, as measured by DCF fluorescence (a). A comparison of the 4T1 cell viability when treated with gradient concentrations of **TMPP-F127** and **Fe-TMPP** (b). Flow cytometric evaluation of 4T1 cell apoptosis by **Fe-TMPP**, **TMPP-F127**, and a PBS using the Annexin V-PI double staining method (c).

The cytotoxicity of **Fe-TMPP** against diverse cell lines including 4T1 (breast cancer), HCT-116 (colorectal cancer), DLD-1 (colorectal cancer), HuH-7 (liver cancer), BXPC3 (pancreatic cancer), PC3 (prostate cancer), and AGS (gastric cancer), were evaluated using either 3-(4,5-dimethylthiazol-2-yl)-2,5-diphenyltetrazolium bromide (MTT) or cell counting kit-8 (CCK-8) assay. As shown in Figure 2b and Figure S15, **Fe-TMPP** exhibited concentration-dependent cytotoxicity against all tested cell lines. The half maximal inhibitory concentration (IC_{50}) values for **Fe-TMPP** were relatively low, down to 0.0975 μM (0.0658 μg mL^{-1}) for AGS and up to 3.97 μM (2.68 μg mL^{-1}) for HCT-116 (Table 2). These IC_{50} values are comparable to cisplatin and to complex formulations that integrate multiple therapeutic modalities. The above results indicate that **Fe-TMPP** exhibits significant cytotoxicity against a broad spectrum of cancer cell lines.

 doi:10.20944/preprints202404.1891.v1

Table 2. A comparison of the IC_{50} values of cell lines induced by the reported drugs and **Fe-TMPP**.

Drug formulation	Cell line	IC_{50}	Reference
Cisplatin	4T1	7.43 μM	[34]
Cisplatin	MCF7	43.0 μM	[35]
Cisplatin	A549	16.4 μM	[36]
Cisplatin	HT29	24.8 μM	[36]
Fe-TBP	CT26	3.10 μM	[37]
bcc-USINPs	Hep-G2	15.7 μg mL^{-1}	[38]
AE@RBC/Fe NCs	HSC-3	7.80 μM	[39]
Fe-TMPP	HCT-116	3.97 μM	This work[†]
Fe-TMPP	4T1	2.00 μM	This work[†]
Fe-TMPP	HuH-7	3.68 μM	This work[†]
Fe-TMPP	BXPC3	3.11 μM	This work[†]
Fe-TMPP	DLD-1	0.231 μM	This work[†]
Fe-TMPP	PC3	0.213 μM	This work[†]
Fe-TMPP	AGS	0.0975 μM	This work[†]

[†] Corresponding IC_{50} values in μg mL^{-1}: HCT-116 (2.68); 4T1 (1.35); HuH-7 (2.49); BXPC3 (2.10); DLD-1 (0.156); PC3 (0.144); AGS (0.0658).

2.6. Ferroptosis Assay

As noted above, when **Fe-TMPP** is internalized by cancer cells, Fe^{3+} can oxidize GSH to give glutathione disulfide (GSSG) and is concomitantly reduced to Fe^{2+}. The exhaustion of GSH in these cells can downregulate the expression of glutathione peroxidase 4 (GPX4), making the cell membrane phospholipid more susceptible to peroxidation.[40,41] GSH depletion and phospholipid peroxidation are two characteristic features of ferroptosis, a novel form of iron-dependent programmed cell death.[40,41] We therefore examined the possibility of ferroptosis induced by **Fe-TMPP** using 4T1 cell line as a representative. Phospholipid peroxidation levels of 4T1 cells were measured using C11-BODIPY (BODIPY™ 581/591 C11) as a fluorescent probe as observed under confocal laser scanning microscopy (Figure 3).[42] We also used DAPI to stain the nucleus of the cells. The cells treated with **Fe-TMPP** showed significantly stronger lipid peroxidation than those treated with **TMPP-F127** or PBS. In addition, lipid peroxidation can be inhibited by the presence of ROS scavengers, such as ferrostatin-1 (Fer-1), liproxstatin-1, and vitamin E.[14,43] In the present experiments, lipid peroxidation was completely inhibited by the introduction of Fer-1, as indicated by the restoration of the red emission of C11-BODIPY. These results indicated that **Fe-TMPP** can induce ferroptosis for cancer treatment. Flow cytometry using Annexin-V/PI double staining further confirmed that 4T1 cells treated with **Fe-TMPP** showed obviously late apoptosis relative to **TMPP-F127** and PBS-treated cells, supporting this alternative cell-death mechanism (Figure 2c).[44,45]

 doi:10.20944/preprints202404.1891.v1

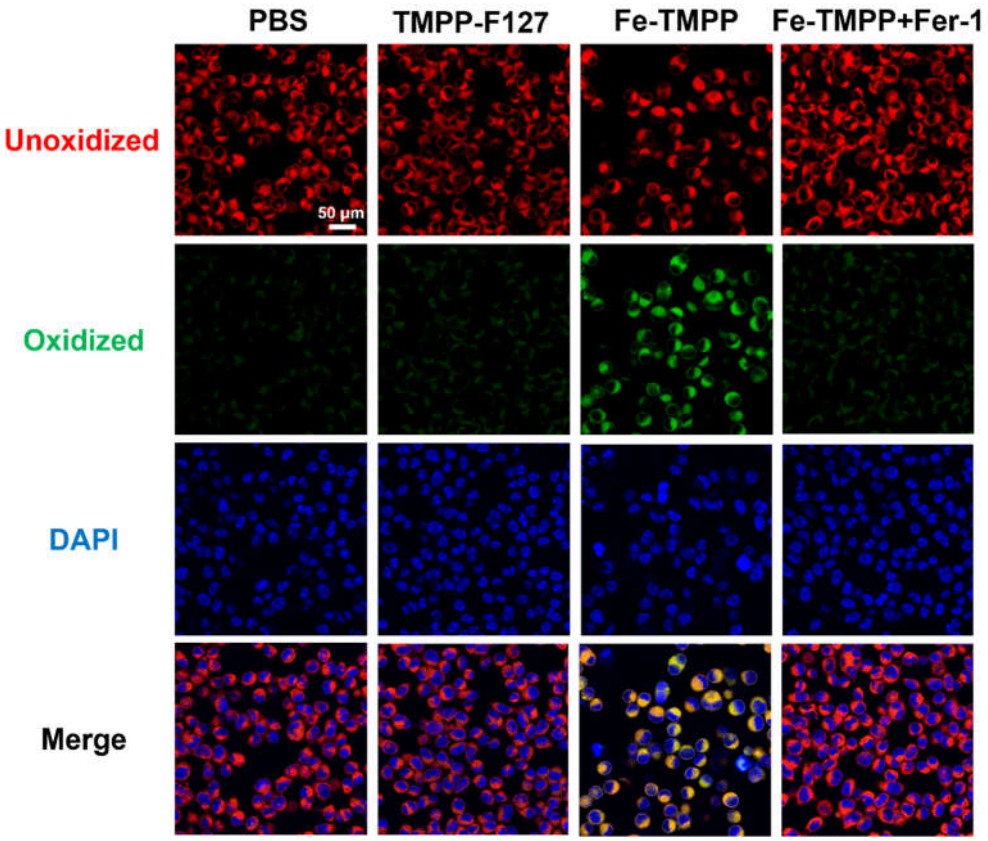

Figure 3. The confocal laser scanning microscopic images of the accumulation of lipid peroxidation in 4T1 cells when treated with PBS control, **TMPP-F127**, **Fe-TMPP**, and **Fe-TMPP** in the presence of Fer-1 as the ferroptosis inhibitor using C11- BODIPY as the fluorescent probe.

3. Materials and Methods

3.1. General

Ligand H_2TMPP was synthesized as described in our previous reports.[18] 3-Aldehyde-6-methylpyridine (>98%, Macklin), ferric chloride hexahydrate (99%, Macklin), pluronic F-127 (average molecular weight 2000, Sigma-Aldrich), 1,3-diphenylisobenzofuran (DPBF) (97%, Acros), 3,3′,5,5′-tetramethylbenzidine (TMB) (99%, Shanghai Yuanye Bio-Technology Co., Ltd.), hydrogen peroxide (H_2O_2, 30%) (Yike Biological Technology Co., Ltd.) were obtained directly from commercial sources and used as received. Pyrrole (>95%, Macklin) was freshly distilled before use.

HCT-116, HuH-7, BXPC3, DLD-1, PC3, AGS, and 4T1 cell lines were purchased from the Shanghai Institute of Cell Biology, Chinese Academy of Sciences. Phosphate buffer solution (PBS), and fetal bovine serum (FBS) supplemented with penicillin and streptomycin were bought from Elabscience Crop (Guangzhou, China). 3-(4,5-Dimethylthiazol-2-yl)-2,5-diphenyltetrazolium bromide (MTT) was purchased from Beijing Solarbio Science & Technology Co., Ltd. The cell counting kit-8 (CCK-8) was commercially available from APEXBIO. 2′,7′-Dichlorodihydrofluorescein diacetate (DCFH-DA) and 4′,6-diamidino-2-phenylindole (DAPI) solution were obtained from Beijing Solarbio Science & Technology Co., LTD. C11-BODIPY$^{581/591}$ was bought from Invitrogen Corp. Ferrostatin-1 (Fer-1) was bought from Yike Biological Technology Co., LTD (Guangzhou, China). The Annexin FITC/PI apoptosis detection kit was purchased from Elabscience Crop.

Fourier transform infrared (FT-IR) spectra were recorded on a Bruker VERTEX 70+HYPERION 2000 spectrometer. UV-Vis absorption spectra were obtained on a Varian Cary-50 UV-Visible spectrophotometer (Varian, Inc., Palo Alto, CA, USA). X-ray photoelectron spectroscopy (XPS) was conducted on an EXCALAB 250 XI X-ray photoelectron spectrometer (Thermo Scientific, Waltham, MA, USA). The EPR measurement was conducted by a Bruker EMXnano spectrometer with DMPO

 doi:10.20944/preprints202404.1891.v1

as the spin-trapping agent. The optical density (OD) values were collected using a TECAN M1000PRO microplate reader (Tecan, Switzerland). The flow cytometry was performed using a BD FACS Caliber instrument (BD Biosciences, San Jose, USA). The transmission electron microscopic (TEM) images were obtained by dropping the sample in water onto a copper net under a HITACHI HT7700 transmission electron microscope. Zeta potentials were measured on an LA-95052 laser particle size analyzer using dynamic light scattering (DLS). The cytotoxicity assay was conducted on a multifunction microplate detector by recording the absorption at 570 nm using a TECAN M1000PRO microplate reader. The cell staining results were observed with a confocal laser scanning microscope (CLSM, AxioObserver A1, Germany). The EDS and elemental mapping diagrams were obtained on the EVO18 scanning electron microscope.

3.2. Synthesis and Characterization of TMPP-F127

Pluronic F-127 (10.6 mg) was introduced to 1 mL of DMSO solution containing H_2TMPP (4.5 mg), and the homogenous mixture formed was then added dropwise into 3.5 mL of deionized water with tip sonication. The micelle formed was dialyzed using a dialysis bag (molecular weight cut-off of 2000 Da) for 24 hours to obtain **TMPP-F127**. TEM indicated that the particle sizes for **TMPP-F127** were 170 ± 25 nm (Figure S12), which is conducive to cellular uptake.

3.3. Synthesis and Characterization of Fe-TMPP

$FeCl_3 \cdot 6H_2O$ (2.4 mg, 0.009 mmol) and H_2TMPP (2 mg, 0.003 mmol) in 2 mL of $CHCl_3$/EtOH (v : v = 3 : 1) were added into a Pyrex glass tube, followed by HAc (50 μL) as a regulator. The resulting mixture was then transferred to a programmable oven, heated to 120°C over 4 h, and maintained at that temperature for 48 h, before cooling to room temperature over 24 h to yield purple block crystals of **Fe-TMPP**, which were collected by filtration, washed thoroughly with anhydrous ether and dried *in vacuo*. Yield: 0.84 mg, 24.2% based on Fe. Anal. Calcd (%) for $C_{44}H_{34}Cl_9Fe_3N_8$: C 45.50%, H 2.95%, N 9.65%; found: C 41.87%, H 2.74%, N 8.70%, corresponding to **Fe-TMPP**·$CHCl_3$ (C 42.20%, H 2.75%, N 8.75%). FT-IR (KBr disc, cm^{-1}): 3372(w), 2521(w), 2162(w), 2029(w), 1607(m), 1552(m), 1458(m), 1377(w), 1329(w), 1288(s), 1258(w), 1204(m), 1139(s), 1085(m), 1047(m), 997(vs), 890(w), 854(w), 801(vs), 744(s), 721(s), 662(m), 624(w).

3.4. Single Crystal X-Ray Crystallography

Data collections were performed on a Bruker APEX II CCD X-ray diffractometer using Mo Kα (λ = 0.71073 Å) irradiation. Refinement and reduction of the collected data were achieved using the program Bruker SAINT and absorption corrections performed using a multi-scan method.[46] Crystal structures were solved by direct methods and refined on F^2 by full-matrix least-squares techniques with *SHELXTL-2016*.[47]

For **Fe-TMPP**, the $[Fe^{III}Cl_4]^-$ anion displays a conformational disorder with a relative ratio of 0.73 : 0.27 refined for the disordered domains. The $[Fe^{III}Cl(TMPPH_2)]^{2+}$ cation also has two conformations due to the presence of 'sit-atop' Fe^{3+}, and the disorder is about the center of the porphyrin ligand. Thus, the occupancy factor of the coordinated FeCl moiety was fixed at 0.5. For the porphyrin ligand, only two pyridyl groups were protonated to balance the charge of the anion. The protonation of half of the four pyridyls can also be judged from the packing of the molecules. In the packing diagram, two pyridyls were brought to proximity by an N-H···N bond, thereby excluding the full protonation of the pyridyls and corroborating the charge counting. A small amount of spatially delocalized electron density in the lattice was found but acceptable refinement results could not be obtained for this electron density. The solvent contribution was then modeled using SQUEEZE in the Platon program suite.[48]

Crystallographic data for **Fe-TMPP** have been deposited in the Cambridge Crystallographic Data Center (CCDC) as supplementary publication number 2330690. These data can be obtained free of charge from the CCDC via www.ccdc.cam.ac.uk/data_request/cif or from the Supporting Information. A summary of the key crystallographic data for **Fe-TMPP** is listed in Table 1.

 doi:10.20944/preprints202404.1891.v1

3.5.•. OH Detection

Different concentrations of **Fe-TMPP** were added to a TMB solution containing 100 μM H_2O_2. After reacting for 3 hours at room temperature, the solution was centrifuged to remove the influence of nanoparticles on absorbance. The ultraviolet absorption curve of the supernatant at 652 nm was determined.

3.6.1. O_2 Detection

Identical concentrations of DPBF were added to aqueous solutions of **TMPP-F127** and **Fe-TMPP** relative to the concentration of TMPP, to give uniform mixtures with the concentration of DPBF and TMPP being 33 μg mL^{-1} and 7 μg mL^{-1}, respectively. The solutions were then irradiated by a laser (650 nm, 25 mW cm^{-2}). After each irradiation for 30 seconds, and absorption of DPBF was immediately measured. By monitoring the decreasing rate of the ultraviolet absorption peak at 416 nm, the $^1O_2$ generation capacities of these materials could be evaluated.

3.7. MTT or CCK-8 Cytotoxicity Assay

The MTT assay of 4T1 cells is detailed as an example. The 4T1 cell line was cultured in RPMI 1640 media supplemented with 10% FBS and 1% penicillin-streptomycin at 37°C in 5% CO_2. Cells grew as a monolayer and were detached upon confluence using trypsin (0.5% w/v in PBS). The cells were harvested from the cell culture medium by incubating in trypsin solution for 2 min, and then centrifuged with the supernatant subsequently discarded. A 3 mL portion of serum-supplemented cell culture medium was added to neutralize any residual trypsin. The cells were re-suspended in serum-supplemented RPMI 1640 at a concentration of 5×10^4 cells/mL. Cells were cultured at 37°C and 5% CO_2 for the MTT studies.

4T1 cells were inoculated into 96-well plates (5×10^3 cells per well) and incubated for 24 h. After 24 h of incubation, the cells were treated with different concentrations of drugs for 24 h, and upon completion of the treatment, the MTT solution was added and incubated for 4 h, and DMSO was added and shocked for 15 min. The cell viability was determined using an enzyme marker.

The relative cell viability (%) related to control cells was calculated by the following equation:

$$V\% = \frac{[A]_{experimental} - [A]_{blank}}{[A]_{control} - [A]_{blank}} \times 100\%$$

wherein $V\%$ is the percentage of cell viability, $[A]_{experimental}$ is the absorbance of the wells culturing the treated cells, $[A]_{blank}$ is the absorbance of the blank, and $[A]_{control}$ is the absorbance of the wells culturing untreated cells.

The cell viability data for HCT-116 (CCK-8), DLD-1 (CCK-8), HuH-7 (CCK-8), BXPC3 (CCK-8), PC3 (CCK-8), and AGS (CCK-8) were obtained in a similar manner using protocols listed in Table S1.

3.8. Intracellular ROS Detection

4T1 cells were inoculated in 12-well plates (1×10^5 cells per well), incubated for 24 h and then treated with different drugs for 24 h. After completion of the treatment, the cells were treated with DCFH-DA, and the cellular reactive oxygen species results were determined using an inverted fluorescence microscopy.

3.9. Flow Cytometric Apoptosis Assay

4T1 cells were inoculated in 6-well plates (3×10^5 cells per well) and incubated for 24 h. After 24 h of incubation, the cells were treated with different drugs for 24 h. After the completion of the treatment, the cells were processed using an Annexin V-FITC/PI apoptosis kit, and the results of apoptosis were determined using flow cytometry.

 doi:10.20944/preprints202404.1891.v1

3.10. Ferroptosis Assay

4T1 cells were inoculated in confocal glass dishes (1×10^5 cells per dish) and incubated for 24 h. Fer-1 (10 μM), an inhibitor of ferroptosis, was added and incubated for 12 h. The cells were then treated with different drugs for 24 h. After the completion of the treatment, the cells were incubated for 30 min with the ferroptosis probe C11-BODIPY$^{581/591}$ (10 μM) and the results of the ferroptosis were observed by CLSM.

4. Conclusions

In this work, a simple Fe(III)-rich coordination complex of **Fe-TMPP** can directly form nanoparticles without the need for extra surface modification or organic-solvent-assisted antisolvent precipitation. The unexpectedly high cytotoxicity originating from ROS alone inspires us to investigate the possibility of other structure analogs based on metal ions such as Cu^{2+} and to further explore the mechanisms of action by examining the sub-organelle locations of these metallodrugs.

Supplementary Materials: The following supporting information can be downloaded at the website of this paper posted on Preprints.org, additional figures and tables.

Author Contributions: Conceptualization, W.H.Z., J.X.C., and Y.M.; methodology, X.W. and J.H.F.; software, W.H.Z. and C.M.Z.; validation, C.M.Z., Z.S.Z., and F.L.C.; formal analysis, X.W. and J.H.F.; data curation, W.H.Z., J.X.C., and D.J.Y.; writing—original draft preparation, X.W. and J.H.F.; writing—review and editing, W.H.Z., J.X.C., Y.M., and D.J.Y.; supervision, W.H.Z.; project administration, W.H.Z. and J.X.C.; funding acquisition, W.H.Z., Y.M., and J.X.C. All authors have read and agreed to the published version of the manuscript.

Funding: This research was funded by the National Natural Science Foundation of China (21871203), the Natural Science Foundation from Guangdong Science and Technology Department of China (2023A1515012633), and the Project of Medical Innovation Application Research of Suzhou (SKY2022094).

Conflicts of Interest: The authors declare no conflict of interest.

References

1. Chu, Z.; Yang, J.; Zheng, W.; Sun, J.; Wang, W.; Qian, H. Recent advances on modulation of H_2O_2 in tumor microenvironment for enhanced cancer therapeutic efficacy. *Coord. Chem. Rev.* **2023**, *481*, 215049.
2. Wang, Y.; Gao, F.; Li, X.; Niu, G.; Yang, Y.; Li, H.; Jiang, Y. Tumor microenvironment-responsive Fenton nanocatalysts for intensified anticancer treatment. *J. Nanobiotechnology* **2022**, *20*, 69.
3. Zou, Y.-M.; Li, R.-T.; Yu, L.; Huang, T.; Peng, J.; Meng, W.; Sun, B.; Zhang, W.-H.; Jiang, Z.-H.; Chen, J., et al. Reprogramming of the tumor microenvironment using a PCN-224@IrNCs/d-Arg nanoplatform for the synergistic PDT, NO, and radiosensitization therapy of breast cancer and improving anti-tumor immunity. *Nanoscale* **2023**, *15*, 10715−10729.
4. Li, W.; Li, R.; Ye, Q.; Zou, Y.; Lu, X.; Zhang, W.; Chen, J.; Zhao, Y. Mn_3O_4 nanoshell coated metal–organic frameworks with microenvironment-driven O_2 production and GSH exhaustion ability for enhanced chemodynamic and photodynamic cancer therapies. *Adv. Healthc. Mater.* **2023**, *12*, 2202280.
5. Huang, N.; Tang, X.-Y.; Meng, W.; Lai, Y.-H.; Zhou, X.; Yu, X.-Z.; Zhang, W.-H.; Chen, J.-X. Immunogenic radiation therapy for enhanced antitumor immunity via a core–shell nanosensitizer-mediated immunosuppressive tumor microenvironment modulation. *ACS Nano* **2023**, *17*, 19853−19864.
6. Hou, Y.-K.; Zhang, Z.-J.; Li, R.-T.; Peng, J.; Chen, S.-Y.; Yue, Y.-R.; Zhang, W.-H.; Sun, B.; Chen, J.-X.; Zhou, Q. Remodeling the tumor microenvironment with core–shell nanosensitizer featuring dual-modal imaging and multimodal therapy for breast cancer. *ACS Appl. Mater. Interfaces* **2023**, *15*, 2602−2616.
7. Pan, W.-L.; Tan, Y.; Meng, W.; Huang, N.-H.; Zhao, Y.-B.; Yu, Z.-Q.; Huang, Z.; Zhang, W.-H.; Sun, B.; Chen, J.-X. Microenvironment-driven sequential ferroptosis, photodynamic therapy, and chemotherapy for targeted breast cancer therapy by a cancer-cell-membrane-coated nanoscale metal-organic framework. *Biomaterials* **2022**, *283*, 121449.
8. Zhang, Y.; Yu, W.; Chen, M.; Zhang, B.; Zhang, L.; Li, P. The applications of nanozymes in cancer therapy: based on regulating pyroptosis, ferroptosis and autophagy of tumor cells. *Nanoscale* **2023**, *15*, 12137−12156.
9. Wen, Y.; Chen, X.; Zhu, X.; Gong, Y.; Yuan, G.; Qin, X.; Liu, J. Photothermal-chemotherapy integrated nanoparticles with tumor microenvironment response enhanced the induction of immunogenic cell death for colorectal cancer efficient treatment. *ACS Appl. Mater. Interfaces* **2019**, *11*, 43393−43408.

 doi:10.20944/preprints202404.1891.v1

10. Huang, N.; Qian, A.; Zou, Y.; Lin, M.; Pan, W.; Chen, M.; Meng, W.; Zhang, W.; Chen, J. Immunogenic radiation therapy for enhanced anti-tumor immunity via core-shell nanocomposite-mediated multiple strategies. *Theranostics* **2023**, *13*, 4121−4137.
11. Liu, J.; Kang, D.W.; Fan, Y.; Nash, G.T.; Jiang, X.; Weichselbaum, R.R.; Lin, W. Nanoscale covalent organic framework with staggered stacking of phthalocyanines for mitochondria-targeted photodynamic therapy. *J. Am. Chem. Soc.* **2024**, *146*, 849−857.
12. Sun, Q.; Yang, J.; Shen, W.; Lu, H.; Hou, X.; Liu, Y.; Xu, Y.; Wu, Q.; Xuan, Z.; Yang, Y., et al. Engineering mitochondrial uncoupler synergistic photodynamic nanoplatform to harness immunostimulatory pro-death autophagy/mitophagy. *Biomaterials* **2022**, *289*, 121796.
13. Ke, L.; Wei, F.; Xie, L.; Karges, J.; Chen, Y.; Ji, L.; Chao, H. A biodegradable iridium(III) coordination polymer for enhanced two-photon photodynamic therapy using an apoptosis–ferroptosis hybrid pathway. *Angew. Chem. Int. Ed.* **2022**, *61*, e202205429.
14. Yuan, H.; Han, Z.; Chen, Y.; Qi, F.; Fang, H.; Guo, Z.; Zhang, S.; He, W. Ferroptosis photoinduced by new cyclometalated iridium(III) complexes and its synergism with apoptosis in tumor cell inhibition. *Angew. Chem. Int. Ed.* **2021**, *60*, 8174−8181.
15. Liu, Z.; Liu, S.; Liu, B.; Bian, Y.; Yuan, M.; Yang, C.; Meng, Q.; Chen, C.; Ma, P.a.; Lin, J. Fe(III)-naphthazarin metal–phenolic networks for glutathione-depleting enhanced ferroptosis–apoptosis combined cancer therapy. *Small* **2023**, *19*, 2207825.
16. Meda, L.; Ranghino, G.; Moretti, G.; Cerofolini, G.F. XPS detection of some redox phenomena in Cu-zeolites. *Surf. Interface Anal.* **2002**, *33*, 516−521.
17. Li, Q.; Xu, B.-W.; Zou, Y.-M.; Niu, R.-J.; Chen, J.-X.; Zhang, W.-H.; Young, D.J. Nanoscale two-dimensional Fe^{II}- and Co^{II}-based metal−organic frameworks of porphyrin ligand for the photodynamic therapy of breast cancer. *Molecules* **2023**, *28*, 2125.
18. Niu, R.-J.; Zhou, W.-F.; Liu, Y.; Yang, J.-Y.; Zhang, W.-H.; Lang, J.-P.; Young, D.J. Morphology-dependent third-order optical nonlinearity of a 2D Co-based metal–organic framework with a porphyrinic skeleton. *Chem. Commun.* **2019**, *55*, 4873−4876.
19. Valicsek, Z.; Horváth, O. Application of the electronic spectra of porphyrins for analytical purposes: The effects of metal ions and structural distortions. *Microchem. J.* **2013**, *107*, 47−62.
20. Basalla, A.J.; Kendrick, B.S. Correcting ultraviolet-visible spectra for baseline artifacts. *J. Pharm. Sci.* **2023**, *112*, 3240−3247.
21. Zhang, Q.; Peng, X.; Nie, Y.; Zheng, Q.; Shangguan, J.; Zhu, C.; Bustillo, K.C.; Ercius, P.; Wang, L.; Limmer, D.T., et al. Defect-mediated ripening of core-shell nanostructures. *Nat. Commun.* **2022**, *13*, 2211.
22. Pochapski, D.J.; Carvalho dos Santos, C.; Leite, G.W.; Pulcinelli, S.H.; Santilli, C.V. Zeta potential and colloidal stability predictions for inorganic nanoparticle dispersions: Effects of experimental conditions and electrokinetic models on the interpretation of results. *Langmuir* **2021**, *37*, 13379−13389.
23. Howard, M.D.; Lu, X.; Jay, M.; Dziubla, T.D. Optimization of the lyophilization process for long-term stability of solid–lipid nanoparticles. *Drug Dev. Ind. Pharm.* **2012**, *38*, 1270−1279.
24. Hussain, Z.; Rahman, S. Storage stabilisation of albumin-loaded chitosan nanoparticles by lyoprotectants. *Trop. J. Pharm. Res.* **2013**, *2*, 135−142.
25. Mahesh, K.V.; Singh, S.K.; Gulati, M. A comparative study of top-down and bottom-up approaches for the preparation of nanosuspensions of glipizide. *Powder Technol.* **2014**, *256*, 436−449.
26. Zhao, X.; Wang, W.; Zu, Y.; Zhang, Y.; Li, Y.; Sun, W.; Shan, C.; Ge, Y. Preparation and characterization of betulin nanoparticles for oral hypoglycemic drug by antisolvent precipitation. *Drug Deliv.* **2014**, *21*, 467−479.
27. Yuan, B.; Chou, H.-L.; Peng, Y.-K. Disclosing the origin of transition metal oxides as peroxidase (and catalase) mimetics. *ACS Appl. Mater. Interfaces* **2022**, *14*, 22728−22736.
28. Li, R.-T.; Zhu, Y.-D.; Li, W.-Y.; Hou, Y.-K.; Zou, Y.-M.; Zhao, Y.-H.; Zou, Q.; Zhang, W.-H.; Chen, J.-X. Synergistic photothermal-photodynamic-chemotherapy toward breast cancer based on a liposome-coated core–shell AuNS@NMOFs nanocomposite encapsulated with gambogic acid. *J. Nanobiotechnology* **2022**, *20*, 212.
29. Cacaccio, J.; Durrani, F.; Cheruku, R.R.; Borah, B.; Ethirajan, M.; Tabaczynski, W.; Pera, P.; Missert, J.R.; Pandey, R.K. Pluronic F-127: An efficient delivery vehicle for 3-(1′-hexyloxy)ethyl-3-devinylpyropheophorbide-a (HPPH or Photochlor). *Photochem. Photobiol.* **2020**, *96*, 625−635.
30. Entradas, T.; Waldron, S.; Volk, M. The detection sensitivity of commonly used singlet oxygen probes in aqueous environments. *J. Photochem. Photobiol. B, Biol.* **2020**, *204*, 111787.
31. Çol, S.; Emirik, M.; Alım, Z.; Baran, A. Physical–chemical studies of new, versatile carbazole derivatives and zinc complexes: Their synthesis, investigation of in vitro inhibitory effects on α-glucosidase and human erythrocyte carbonic anhydrase I and II isoenzymes. *Appl. Organomet. Chem.* **2022**, *36*, e6799.
32. Rozenberga, L.; Skinner, W.; Lancaster, D.G.; Bloch, W.M.; Blencowe, A.; Krasowska, M.; Beattie, D.A. A europium metal–organic framework for dual Fe^{3+} ion and pH sensing. *Sci. Rep.* **2022**, *12*, 11982.
33. Yuan, F.-L.; Yuan, Y.-Q.; Chao, M.-Y.; Young, D.J.; Zhang, W.-H.; Lang, J.-P. Deciphering the structural relationships of five Cd-based metal–organic frameworks. *Inorg. Chem.* **2017**, *56*, 6522−6531.

 doi:10.20944/preprints202404.1891.v1

34. Zhu, H.; Li, Q.; Shi, B.; Ge, F.; Liu, Y.; Mao, Z.; Zhu, H.; Wang, S.; Yu, G.; Huang, F., et al. Dual-emissive platinum(II) metallacage with a sensitive oxygen response for imaging of hypoxia and imaging-guided chemotherapy. *Angew. Chem. Int. Ed.* **2020**, *59*, 20208−20214.
35. Zhao, H.; Xu, J.; Huang, W.; Zhao, Y.; Yang, X. Thermosensitive nanogels with cross-linked Pd(II) ions for improving therapeutic effects on platinum-resistant cancers via intratumoral formation of hydrogels. *Chem. Mater.* **2019**, *31*, 5089−5103.
36. Yue, Z.; Wang, H.; Li, Y.; Qin, Y.; Xu, L.; Bowers, D.J.; Gangoda, M.; Li, X.; Yang, H.-B.; Zheng, Y.-R. Coordination-driven self-assembly of a Pt(IV) prodrug-conjugated supramolecular hexagon. *Chem. Commun.* **2018**, *54*, 731−734.
37. Lan, G.; Ni, K.; Xu, Z.; Veroneau, S.S.; Song, Y.; Lin, W. Nanoscale metal-organic framework overcomes hypoxia for photodynamic therapy primed cancer immunotherapy. *J. Am. Chem. Soc.* **2018**, *140*, 5670−5673.
38. Liang, H.; Wu, X.; Zhao, G.; Feng, K.; Ni, K.; Sun, X. Renal clearable ultrasmall single-crystal Fe nanoparticles for highly selective and effective ferroptosis therapy and immunotherapy. *J. Am. Chem. Soc.* **2021**, *143*, 15812−15823.
39. Wu, M.; Ling, W.; Wei, J.; Liao, R.; Sun, H.; Li, D.; Zhao, Y.; Zhao, L. Biomimetic photosensitizer nanocrystals trigger enhanced ferroptosis for improving cancer treatment. *J. Control. Release* **2022**, *352*, 1116−1133.
40. Chen, Z.; Wang, W.; Abdul Razak, S.R.; Han, T.; Ahmad, N.H.; Li, X. Ferroptosis as a potential target for cancer therapy. *Cell Death Dis.* **2023**, *14*, 460.
41. Lei, G.; Zhuang, L.; Gan, B. Targeting ferroptosis as a vulnerability in cancer. *Nat. Rev. Cancer* **2022**, *22*, 381−396.
42. Drummen, G.P.C.; van Liebergen, L.C.M.; Op den Kamp, J.A.F.; Post, J.A. C11-BODIPY581/591, an oxidation-sensitive fluorescent lipid peroxidation probe: (micro)spectroscopic characterization and validation of methodology. *Free Radic. Biol. Med.* **2002**, *33*, 473−490.
43. Li, J.; Cao, F.; Yin, H.-l.; Huang, Z.-j.; Lin, Z.-t.; Mao, N.; Sun, B.; Wang, G. Ferroptosis: past, present and future. *Cell Death Dis.* **2020**, *11*, 88.
44. Liang, X.; Chen, M.; Bhattarai, P.; Hameed, S.; Tang, Y.; Dai, Z. Complementing cancer photodynamic therapy with ferroptosis through iron oxide loaded porphyrin-grafted lipid nanoparticles. *ACS Nano* **2021**, *15*, 20164−20180.
45. Wan, X.; Song, L.; Pan, W.; Zhong, H.; Li, N.; Tang, B. Tumor-targeted cascade nanoreactor based on metal–organic frameworks for synergistic ferroptosis–starvation anticancer therapy. *ACS Nano* **2020**, *14*, 11017−11028.
46. Sheldrick, G.M. SADABS (Version 2.03): Program for empirical absorption correction of area detector data; University of Göttingen, Germany. **1996**.
47. Sheldrick, G.M. Crystal structure refinement with SHELXL. *Acta Crystallogr., Sect. C* **2015**, *71*, 3−8.
48. Spek, A.L. PLATON SQUEEZE: A tool for the calculation of the disordered solvent contribution to the calculated structure factors. *Acta Crystallogr., Sect. C* **2015**, *71*, 9−18.